Advanced Manufacturing for Electrosynthesis of Fuels and Chemicals from CO$_2$

Advanced Manufacturing for Electrosynthesis of Fuels and Chemicals from CO_2

Daniel Corral[1,2,†], Jeremy T. Feaster[3,†], Sadaf Sobhani[4], Joshua R. DeOtte[1], Dong Un Lee[2],
Andrew A. Wong[1], Julie Hamilton[1], Victor A. Beck[4], Amitava Sarkar[2,3,5], Christopher Hahn[6,*],
Thomas F. Jaramillo[2,6,*], Sarah E. Baker[3,*], and Eric B. Duoss[1,*]

[1] Materials Engineering Division, Lawrence Livermore National Laboratory, Livermore, CA 94550, United States

[2] SUNCAT Center for Interface Science and Catalysis, Department of Chemical Engineering, Stanford University, Stanford, CA 94305, USA

[3] Materials Science Division, Lawrence Livermore National Laboratory, Livermore, CA 94550, United States

[4] Computational Engineering Division, Lawrence Livermore National Laboratory, Livermore, CA 94550, United States

[5] Total EP Research & Technology USA, LLC., Houston, TX 77002, USA

[6] SUNCAT Center for Interface Science and Catalysis, SLAC National Accelerator Laboratory, Menlo Park, CA 94025, USA

† These authors contributed equally to this work.

*Correspondence: chahn@slac.stanford.edu, jaramillo@stanford.edu, baker74@llnl.gov, and duoss1@llnl.gov

Abstract

Advanced manufacturing (AM) represents an appealing approach for creating novel electrochemical systems for chemicals synthesis. In this work, we demonstrate AM for rapid development and testing for improved performance for the carbon dioxide reduction reaction across an evolution of vapor-fed reactor designs. In our final design, we observe activation- and mixed- control regimes for a variety of operating conditions via inlet CO_2 flow rate and electrochemical potential. Furthermore, we define a dimensionless number (Da) to identify mass transport regimes by exploring the impact of hypothesized underlying mass transport mechanisms, including consumption of CO_2 via OH^-, increased local temperatures, and partial penetration of electrolyte into gas diffusion layer. The accelerated pace of reactor design and development led to high geometric current densities (500 mA cm^{-2}), heightened selectivity (85.5% FE C_{2+} products), and increased carbon dioxide conversion (16.6%) and cathodic energy efficiency (56.3% CO_2R). Using AM vapor-fed reactors, we attain high ethylene (3.67%) and record ethanol (3.66%) yields compared to the literature. This work underscores the promise of AM for accelerating reactor design, understanding of governing phenomena, and improving the performance of catalytic systems.

Broader Impact

Advanced manufacturing as a method to create novel electrochemical reactors opens the door to many different energy technologies ahead. In combination with CO_2 electroreduction, excess renewable energy can effectively be stored as fuels and additives, as well as non-fossil derived consumer and industrial chemicals (e.g. monomers for polymerization and constructions materials) for longer-term sequestration of CO_2 out of environment. Reactor design and manufacturing is central to achieving progress toward these goals; understanding of the mass transport phenomena occurring within the reactor must be developed to build more efficient and effective systems. The high activity, selectivity, cathodic energy efficiency, CO_2 single-pass conversion and product yields achieved in this work were accomplished with a generic Cu catalyst in bulk neutral pH. This highlights the potential of this methodology in design optimization and enhanced system performance when sophisticated catalysts and/or reaction systems are employed. AM reactors represent a significant step towards de-risking scale-up and optimization of this game-changing technology while developing design metrics that can promote commercial feasibility. This work also validates that cost-effective AM techniques can be utilized for rapid production of modular system components with high precision and reproducibility that are necessary for future industrial deployment.

Keywords

Advanced manufacturing, CO_2 reduction, 3D printing, electrocatalysis, reactor design, ethylene, ethanol

Introduction

The accelerating need to mitigate global emissions of CO_2 has driven significant advancements in designing systems and strategies that transition towards a sustainable future.[1–3] However, a growing global population continues to rely on fossil-derived sources for power, chemicals, agriculture, and transportation sectors.[4] Converting this CO_2 to fuels and chemical feedstocks can be an effective way to reduce the CO_2 footprint of many conventional chemical processes, thus promoting a circular carbon-economy.[5] Considering the cheap (~ \$0.02 kWh^{-1}) and sometimes free renewable energy generated in certain parts of the world, such energy can be stored by converting CO_2 to synthesis gas, future energy carriers (e.g. fuels and additives), and monomers for polymerization. Thus, electrochemical CO_2 reduction (CO_2R) to produce non-fossil sourced chemical products can be a significant milestone in decarbonizing the chemicals industry.

While there are several challenges associated with scaling up CO_2R, much progress has been made to better understand a variety of complex phenomena and coexisting processes. Aqueous-phase CO_2R, performed in liquid-fed reactors (LFRs) leveraging electrochemical[6–8] as well as photocatalytic[9,10] driving forces, served as the primary platform for investigating selectivity trends and discovering new materials.[11,12] Furthermore, studies in LFRs elucidated the effects of various intermediates, including *COOH[8,13–15], *CO[16,17], and even *C_2O_4[18] in light driven conditions, which aided in our understanding of reaction mechanisms. The transition from LFRs to vapor-fed reactors (VFRs) utilizing gas diffusion electrodes (GDEs) yielded higher performance metrics by minimizing the distance between the electrode and bulk vapor CO_2 stream.[19] Previous studies achieved high activity and selectivity towards the production of CO, HCOO$^-$, C_2H_4, and C_2H_5OH by capitalizing on the increased complexity and tunability of GDEs.[20] Despite recent

81 advances, it is unclear whether the understanding of kinetic mechanisms and mass transport

82 phenomena in LFRs translates to industrially relevant current densities observed in VFRs.

83   To date, published reports on electrochemical reactors for CO_2 reduction have all focused

84 on components that rely on traditional manufacturing methods which are time- and resource

85 intensive.[21,22] Industrial deployment of CO_2R technology to replace current production volumes of

86 the chemical and petrochemical industry will require manufacturing millions of these system

87 components with high precision and reproducibility for modular electrolyzers. Advanced

88 manufacturing (AM) is a promising approach to overcome these limitations, as it allows for rapid

89 prototyping and iteration of reactor components and parts with submicron control.[23,24] These

90 advantages of AM have led to novel materials and devices for energy storage,[25] optics,[26] drug

91 delivery[27], and carbon capture applications.[28] However, there have been few studies to date that

92 have employed AM for electrochemical reactor design,[29] and none to date for electrochemical CO_2

93 reduction.

94   For the first time to date, we demonstrate AM for fabrication of CO_2 electrolyzers with

95 increased precision. This enables the rapid prototyping of different system components with

96 conceptual design aspects and corresponding assessment of important design parameters. AM

97 VFRs showcase promising results for CO_2 reduction with an unoptimized electrode, membrane,

98 and electrolyte, including high selectivity for multi-carbon products at high current densities. We

99 identify and evaluate mass transport regimes for various flow rate and electrochemical potential

100 conditions and investigate underlying mass transport mechanisms. Consequently, we propose that

101 for a given reactor and system configuration, the use of the dimensionless Damköhler (Da) number

102 can elucidate regimes based on the proposed mechanisms. Lastly, we introduce yield as a key

103 metric for evaluating performance of CO_2 electrolyzers.

Experimental methods

104

**Reactor manufacturing and catalyst characterization**

105

All experimental data was obtained from 3D-printed VFRs and components based on an informed

106

and iterative reactor design process. Electrochemical reactors (Fig. S1) and electrolyte sparging

107

chambers were first drafted using computer-aided design (CAD) software (AutoCAD Inventor).

108

Each VFR was designed with a 1.4 cm^2 geometric surface area for the cathode, anode, and

109

membrane windows. As gas bubbles formed on the electrodes can influence mass transport and

110

electric field uniformity within the reactor, compartments were designed with a tapered geometry

111

to direct fluid flow for enhanced bubble management (Fig. S3). All components were then printed

112

using a stereolithography (SLA) 3D printer (FormLabs Form2, 25 μm step size); all components

113

were made from a polyacrylate-based commercial resin (Formlabs). After printing, each reactor

114

component was sonicated in an IPA bath for at least 30 minutes to remove any excess or uncured

115

resin, then cured with UV light at 60°C for 60 minutes. The components were then rinsed

116

thoroughly in deionized water before use and rinsed thoroughly between experimental runs.

117

A 275 nm thick layer of Cu was deposited onto ePTFE (Sterlitech) using e-beam physical

118

vapor deposition in a rotating chamber (see Supplemental Information for full details). Scanning

119

electron microscopy (SEM) images reveals the coating of Cu catalyst on top of the ePTFE fibers

120

(Fig. S6). X-ray photoelectron spectroscopy (XPS) validated both cleaned ePTFE and Cu/ePTFE

121

samples (Fig. S7). To identify the facets post-deposition, we performed X-ray diffraction (XRD)

122

and observed Cu(111), Cu(200) and Cu(220) peaks (Fig. S8). Double-layer capacitance was used

123

to measure the electrochemically active surface area (ECSA) of the catalyst (Figure S10); the

124

ECSA measured was similar to those measured other reports.[30–32]

125

126

127   **Electrochemical experiments**

128   All electrochemical experiments were carried out using a multichannel potentiostat (Bio-

129   Logic). An IrO_2 catalyst on a carbon paper electrode (Dioxide Materials) was cut and used as the

130   anode. A Low-Profile silver/silver chloride (Ag/AgCl) electrode (Pine Instruments) was used as

131   the reference electrode and connected to the catholyte compartment of the reactor. A 50μm

132   Sustanion anion exchange membrane (Dioxide Materials) was inserted between the catholyte and

133   anolyte chambers to mitigate the cross-over of impurities and products between the electrodes.

134   Both catholyte and anolyte were recirculated using external 3D-printed chambers (each with a

135   volume of 25 mL) to minimize local accumulation of products. Potentiostatic electrochemical

136   impedance spectroscopy (PEIS) was used to measure the solution resistance (1) between the

137   cathode and the reference electrode, and (2) between the cathode and the anode (Fig. S9).

138   Chronoamperometry (CA) was performed for 5 minutes at a soft overpotential of -0.75 V vs.

139   Ag/AgCl to reduce any oxide on the Cu surface. Finally, chronopotentiometry (CP) was performed

140   at a given current density; the solution resistance was measured every 3 minutes to allow for

141   correction of the voltage drop due to changes in electrolyte conductivity. The average resistance

142   and potential from each run were used for analysis. Each experiment was duplicated to ensure each

143   result was reproducible.

Results and discussion
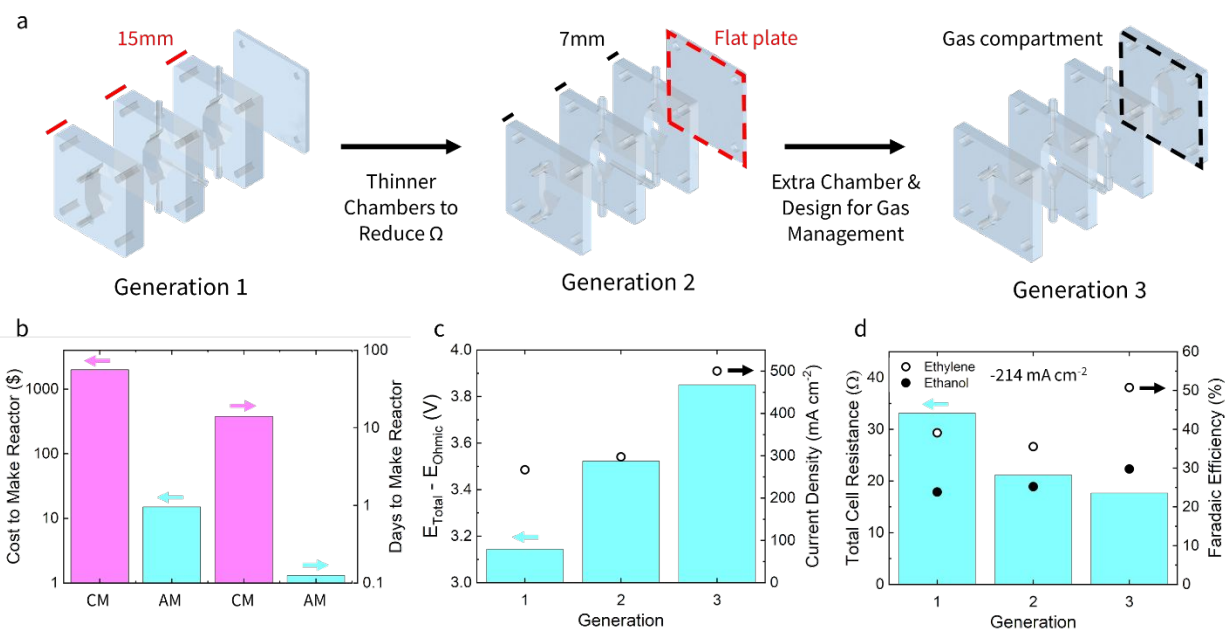
Fig. 1. Advantages of AM for electrochemical reactor design. (a) Schematic representation of three generations of reactors designed for CO_2R with brief description of changes between generations. (b) Order of magnitude advantages of AM over conventional manufacturing (CM) with regards to cost and time to produce electrolyzer. (c) Potential realized at electrodes (represented as the difference of the cell potential and the potential lost to ohmic drop) and maximum current density in each generation. (d) Total cell resistance and Faradaic efficiencies of ethylene and ethanol at a fixed current density for all three generations.

We employed stereolithography 3D printing to develop several generations of vapor-fed electrochemical systems (Fig. 1a). Using AM instead of conventional manufacturing (CM), we reduced the cost and the amount of time to produce each reactor component by several orders of magnitude (Fig. 1b). Several metrics informed the rapid development from Generation 1 to Generation 3: the total cell resistance measured between the cathode and anode, the total cell potential to operate the reactor at 214 mA cm^{-2}, and the current density achieved at a compliance voltage of ±10V (Fig. 1, c and d). Generation 1 reactors had a total cell resistance of 33.1Ω, split between the electrolyte (22.3Ω) and the membrane (10.7Ω), which led to a large voltage drop (~10V at 214 mA cm^{-2}) and a maximum current density of 266 mA cm^{-2}. Informed by these

163   findings, Generation 2 reactors decreased the distance between the electrodes by over half, which

164   consequently reduced the ohmic resistance. Accordingly, Generation 2 reactors exhibited a total

165   cell resistance of 21.2Ω, which represents a 34% decrease from Generation 1; however, the

166   maximum current density achieved only increased to 297 mA cm^{-2}, indicating that ohmic

167   resistance of the electrolyte was not the only limiting factor.

168   The Generation 3 system design connected the cathode gas and catholyte compartments in

169   a 3D-printed sparging chamber, saturating the electrolyte with CO_2 and reducing pH gradients and

170   concentration polarization (Fig. S2). This also eliminated pressure differences between the gas

171   compartments and the liquid compartments, minimizing breakthrough of electrolyte and flooding

172   due to a pressure gradient. Additionally, Generation 3 reactors featured a fourth compartment for

173   removal of oxygen and degassed carbon dioxide[33] from the anode at high current densities and

174   maintained the same distance between the cathode and anode. With these changes to the reactor

175   and system design, Generation 3 reactors achieved a lower cell resistance (17.7Ω), which is

176   primarily the result of a lower bulk pH due to continuous CO_2 saturation. At 214 mA cm^{-2},

177   Generation 3 reactors resulted in a ~5V drop due to ohmic losses, almost 50% less than that of

178   Generation 1 reactors; this generation also exhibited higher Faradaic efficiencies (FE) for ethylene

179   and ethanol. This system reached current densities greater than 500 mA cm^{-2}, establishing the

180   viability of AM for high-rate electrosynthesis from CO_2.

Evaluating performance of AM VFRs for various inlet CO_2 flow rates
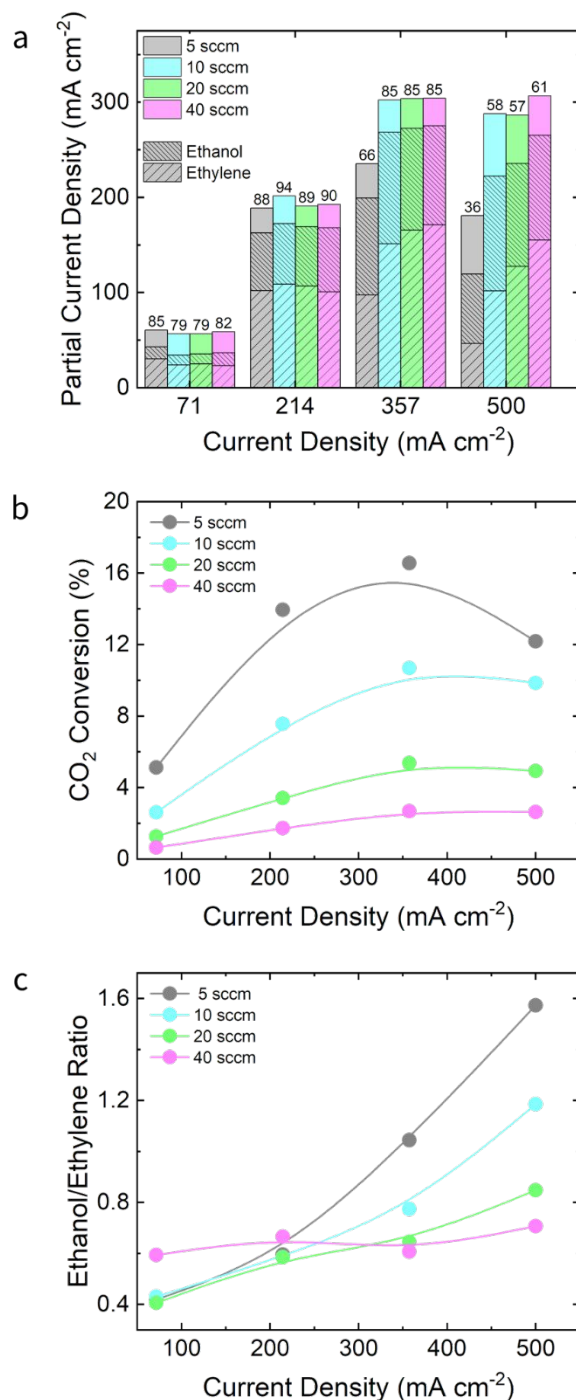
Fig. 2. (a) CO_2R partial current density as a function of total current density for various flow rates. Ethylene and ethanol fractions are shaded. Other CO_2R products (CO, $HCOO^-$, CH_4, CH_3COO^-, CH_3CHO, and C_3H_7OH) are grouped within the unshaded region. The CO_2R Faradaic efficiency corresponding to condition is shown above each stacked column. (b) Electrochemical CO_2 conversion as a function of total current density for various flow rates. (c) Ratio of oxygenates to hydrocarbons as a function of flow rate and current density.

188

189   Building upon the advancements of the Generation 3 reactor, we explored the CO_2R performance

190   in depth for this AM system. We covered a range of CO_2 inlet flow rates of 5, 10, 20, and 40 sccm

191   on a simple Cu/PTFE catalyst and in 1 M $KHCO_3$. For these conditions, we display the current

192   density towards CO_2-reduced products (Fig. 2a) and the corresponding electrochemical CO_2

193   conversion (Fig. 2b). Peak conversion occurs for all flow rate conditions at 357 mA cm^{-2}, with a

194   maximum of 16.5% at 5 sccm. We observed two distinct regimes regarding CO_2 mass transport

195   effects: an activation-controlled regime, which has sufficient transport of CO_2 for electroreduction,

196   and a mixed-controlled regime, where both kinetic and mass transport effects lead to insufficient

197   concentrations of CO_2 throughout catalyst layer.

198   We observe little to no effect of CO_2 flow rate on the activity and selectivity of products at

199   lower current densities ($\leq$ 214 mA cm^{-2}), indicating this regime is activation controlled for all

200   tested flow rates. At higher current densities, electrolytic performance differs with CO_2 flow rate,

201   suggesting that some conditions operate in the mixed-controlled regime. At 357 mA cm^{-2}, the total

202   CO_2R current (~235 mA cm^{-2}) at 5 sccm is lower than that of the other flow rates (~300 mA cm^{-2}

203   ^{2}). For > 10 sccm, there is a positive correlation between ethylene production and CO_2 flow rate,

204   while ethanol production remains unaffected, thus increasing the ratio of ethanol to ethylene (Fig.

205   2c). This trend is opposite of that observed in aqueous systems[16]; we attribute this to dramatic

206   differences in the local environment and available CO_2 between VFRs and LFRs. The selectivity

207   for ethylene at the catalyst surface could be influenced by the diffusion of the gaseous products

208   into the PTFE and out with the effluent gas stream; this diffusion depends on the flow rate of CO_2

209   in the reactor. The diffusion of ethanol into the electrolyte is not sharply influenced by the CO_2

210   gas flow, suggesting the ethanol pathway is preferred when CO_2R is either partially or fully

211   diffusion-controlled. Furthermore, the consistent activity towards ethanol may be influenced by

212   the heterogeneity of active sites[34] and increased absorption of H on Cu.[35]

213   At 500 mA cm^{-2}, we observe a drop in CO_2R current density across flow rates < 40 sccm;

214   this is an extension of the effect seen at 5 sccm and 357 mA cm^{-2}. A decrease in ethylene production

215   corresponds to an increase production of hydrogen and methane, accounting for the remainder of

216   CO_2R current. At higher cathodic potentials, increased adsorption of hydrogen (*H) can suppress

217   conversion of CO_2 to multi-carbon products.[17] Feeding CO_2 at 40 sccm resulted in reaching the

218   mass transport limited current density previously observed at 357 mA cm^{-2}. This clear distinction

219   between activation- and mixed-controlled regimes highlights the importance of both CO_2 inlet

220   flow and applied current density on mass transport effects within electrochemical reactors.

Mass transport limited current density in AM VFRs
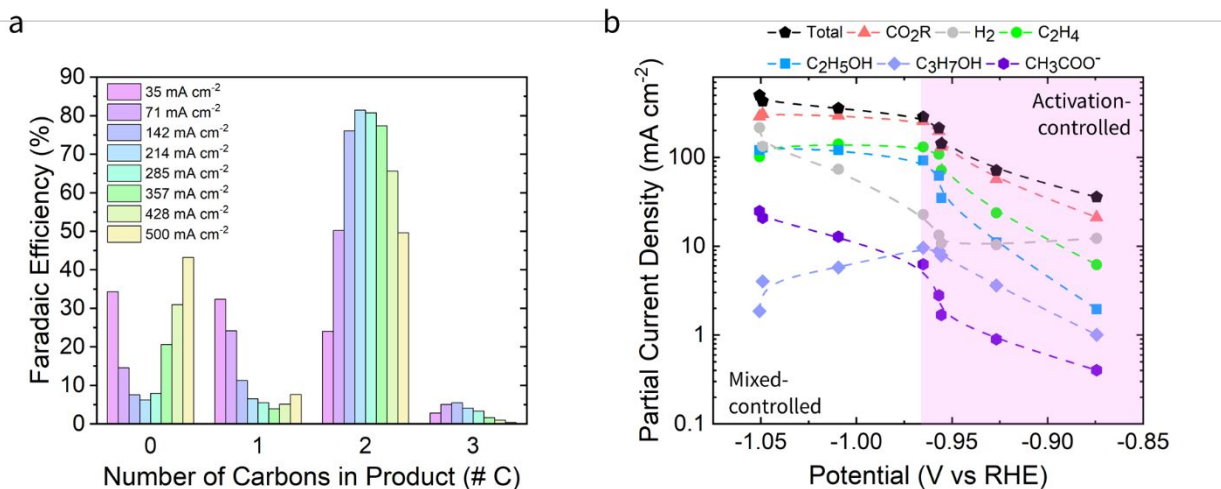
Fig. 3. (a) Selectivity towards 0-carbon (H_2), 1-carbon (CO, HCOO-, CH_4), 2-carbon (C_2H_4, C_2H_5OH, CH_3COO^-, CH_3CHO), and 3-carbon (C_3H_7OH) products at different current densities. (b) Partial current densities of select products and CO_2R, as well as total current density, as a function of applied cathodic potential.

We also investigated the effects of the electrode potential on electrocatalytic performance at 10 sccm CO_2 flow rates. The system demonstrated remarkable selectivity for CO_2R across a wide range of current densities (Fig. 3a), including over 90% FE for CO_2R from 142 mA cm^{-2} to 285 mA cm^{-2}; at 142 mA cm^{-2} we observed the maximum CO_2R cathodic energy efficiency and FE for the system at 49.6% (Fig. S13) and 92.8%, respectively. Total C_{2+} FE reached a maximum of 85.9% FE at 214 mA cm^{-2}, which is one of the highest reported to multi-carbon products for CO_2R; the two major products formed were ethylene (50.7% at 214 mA cm^{-2}) and ethanol (33.9% at 357 mA cm^{-2}). Strikingly, we show here that high selectivity for CO_2R and CO_2 conversion can be achieved in bulk pH-neutral environments with no modifications or additives to either the catalyst or electrolyte. This compares favorably to previous reports using further-developed Cu electrodes and/or operating in alkaline conditions,[32,35–42] while mitigating issues associated with bulk electrolyte consumption of CO_2 that is particularly problematic in alkaline environments and can lead to lower overall system efficiency.[33]

240   Hydrogen, the only zero-carbon product, remained below 8% from 142 to 285 mA cm^{-2},

241   agreeing with previous reports depicting a preference for CO_2R within this current density

242   range.[33,43] At current densities $\leq$ 285 mA cm^{-2}, hydrogen decreased in FE from 34% to 8% while

243   2-carbon products rapidly increased from 24% to 81%; formation of single-carbon products were

244   consistently low in this regime. This inverse relationship is a result from several factors, including

245   sufficient adsorption of *CO[17,43] and *COOH[8,13–15] intermediates on the catalyst surface and

246   favorable kinetics for carbon-carbon coupling.[7,8,44] Furthermore, suppression of HER occurs via

247   an increasing pH in the local environment;[32,33] we predict an increase up to 5 units for pH in our

248   system (Fig. S21).

249   Similar to the results from the flow rate study, we observed both activation-controlled and

250   mixed-controlled regimes based on partial current densities and the corresponding electrochemical

251   potential (Fig. 3b). The potential range from -0.87V to -0.97V vs RHE corresponds to the

252   activation-controlled regime; CO_2R current density increases exponentially as a function of

253   potential, with product activities tracing the behavior of Butler-Volmer kinetics.[45] The partial

254   current densities of the 2-carbon products (C_2H_4, C_2H_5OH, and CH_3COO^-) increase at similar rates

255   in this regime; their slopes suggest the sharing of some reaction pathways and carbonaceous

256   intermediates.[7,12,17,46]

257   A plateau in CO_2R current density of around ~300 mA cm^{-2} is a result of a transition from

258   activation- to mixed-controlled regimes ($\leq$ -0.97V vs. RHE). While ethylene and ethanol current

259   densities reach an asymptote, H_2 and CH_4 partial current densities increase and agree with previous

260   literature (Fig. S12).[12,47,48] This relationship suggests a higher *H coverage on the catalyst surface,

261   increasing the probability of protonating adsorbed single-carbon species. Interestingly, acetate

262   partial current density increases throughout both regimes, suggesting acetate formation may

263   correlate with concentration of OH^-.[49] As the total current density approaches 500 mA cm^{-2}, total

264   CO_2 conversion decreases, suggesting a modified reaction environment that favors hydrogen

265   evolution. At higher overpotentials, an high local pH and lower concentrations of $KHCO_3$ likely

266   result in a dominant proton-donor shift to H_2O.[50] The CO_2 mass transport limitation observed in

267   this region is analogous to results that have been observed in aqueous, liquid-fed CO_2R systems.[12]

268 **CO$_2$ mass transport-limiting phenomena**

269 There are several mass transport phenomena that control how CO$_2$ reaches the catalyst surface in

270 aqueous electrolyte VFRs: diffusion of CO$_{2(g)}$ through the PTFE layer to the catalyst layer,

271 dissolution of CO$_{2(g)}$ into the electrolyte to form CO$_{2(aq)}$, and diffusion of CO$_{2(aq)}$ to the catalyst

272 surface. Many studies show that OH$^-$ production at the cathode and consequent homogenous

273 consumption of CO$_{2(aq)}$ to form carbonate can result in variable reactant concentrations, alter

274 product selectivity, and limit CO$_2$ transport to the catalyst layer.[32,51–54] However, high current

275 densities (> 1 A cm^{-2}) to reduced products in alkaline conditions[40,42] suggest additional mass

276 transport limiting phenomena must be present in these bulk neutral-media, AM VFR systems.
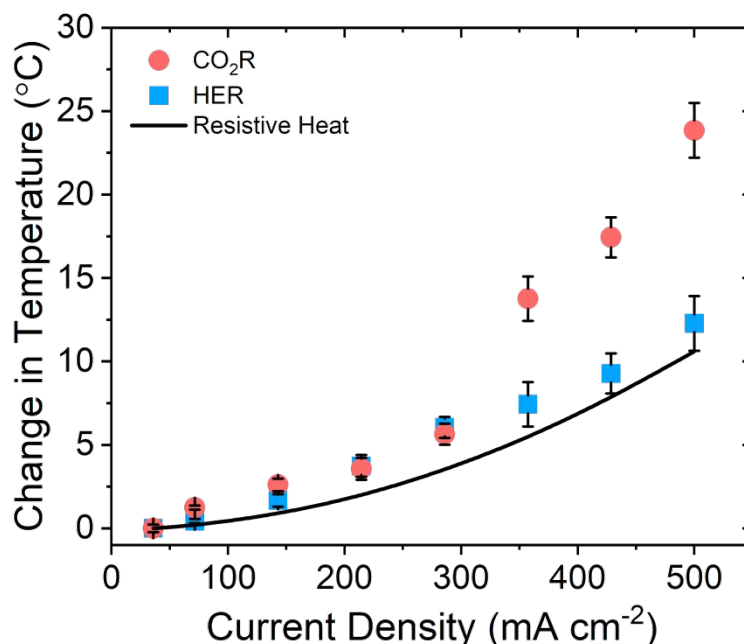
277

278 **Fig. 4.** Measured cathode temperature during electrolysis for CO$_2$R and HER at 10 sccm. Modeling of the expected
279 increase in temperature based on resistive heating is represented as the solid black curve.
280

281 We propose that temperature can change the concentration of CO$_2$ at the gas-liquid

282 interface, contributing to CO$_2$ mass transport limitations. While there is previous literature on the

283   effect of temperature on CO_2R,[55–57] there remains a lack of experimental understanding on how

284   temperature changes within VFRs during CO_2 electrolysis. We measured the temperature change

285   of the catholyte near the cathode surface for both HER and CO_2R (Fig. 4). At current densities <

286   300 mA cm^{-2}, the increase in temperature across the cathode is < 7°C for all experiments; this

287   results from resistive heating of the electrolyte, as seen by the simulated temperature change from

288   the model. As resistive heating is dependent on the applied current and electrolyte resistance, the

289   measured increase in temperature for HER and CO_2R are similar in this range. At current densities

290   > 300 mA cm^{-2}, the increase in temperature is higher in CO_2R (max of ~24°C at 500 mA cm^{-2})

291   than in HER (max of ~12°C at 500 mA cm^{-2}). The exothermic reaction of OH^- with CO_2 and the

292   heats of reaction from all electrochemical reactions at the catalyst surface contribute significantly

293   to the difference in temperature increase.

294   Dynamic changes in temperature change several key variables that can impact CO_2 mass

295   transport. At higher temperatures, the solubility of CO_2 decreases from 33.4 mM at 25°C to 20.0

296   mM at 45°C. Coupled with higher concentrations of OH^- in the electrolyte, this can reduce the

297   amount of CO_2 that is available to the catalyst, leading to a mass transport limited current density

298   for CO_2R. Additionally, temperature increases can change the conductivity of the electrolyte and

299   the diffusion of various species in the aqueous phase; it can also influence the kinetic barriers for

300   CO_2R reaction pathways, which can alter the selectivity of the catalyst and limit the rate of CO_2R

301   at high current densities.
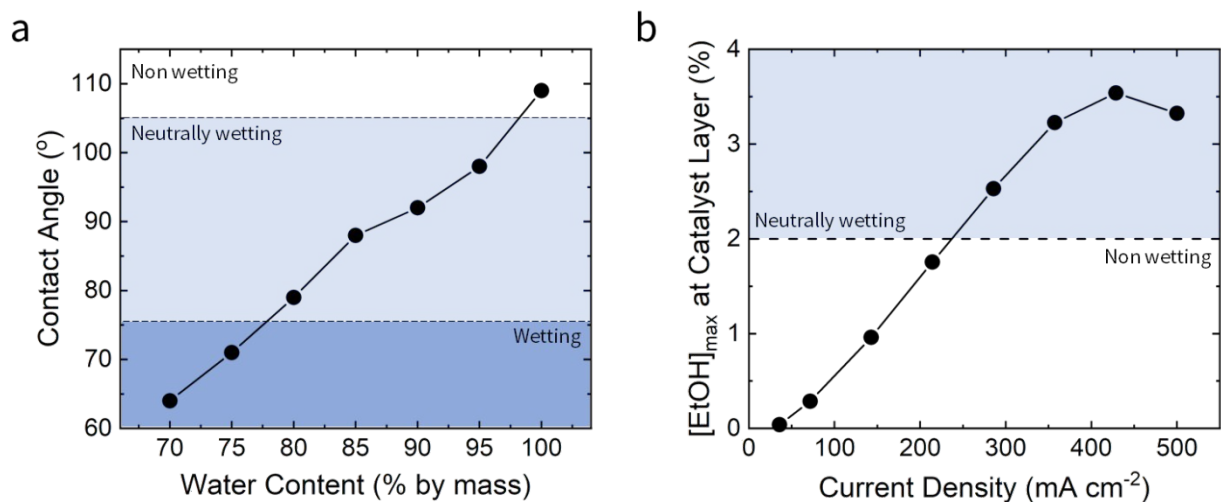
Fig. 5. (a) Contact angle measurements for ethanol/water mixtures on bulk PTFE. This represents a conservative estimate for wetting of electrodes, as the Cu catalyst is more hydrophilic than PFTE. (b) Calculated maximum ethanol concentrations at the gas-liquid-solid interface as a function of total current density. Shaded and unshaded zone represents neutrally wetted and non-wetted regions, respectively.

Additionally, we hypothesize that changes in wettability of the PTFE support can contribute to CO_2 mass transport limitations.[58] Solvent water does not wet the PTFE support and the triple phase interface remains abrupt and close to the cathode.[32] Liquid products (particularly ethanol) that are produced in the catalyst layer can wet the PTFE support by changing the solvent surface tension.[58] Based on contact angle measurements (Fig. 5a), only a small concentration of ~2% (by mass) of ethanol is sufficient to change the hydrophobicity of the PTFE from non-wetting ($\Theta > 105°$) to neutrally wetting ($75° < \Theta < 105°$).[59] We calculate a maximum ethanol concentration of > 3.5% for a range of current densities in our reactor (Fig. 5b); this suggests that the electrolyte could begin penetrating the neutrally wet PTFE interface. Electrolyte penetrating the PTFE could block pores and extend the gas-electrolyte interface, inhibiting CO_2 mass transfer.[51,58] It is challenging to determine the exact depth of electrolyte penetration due to species transport, local pressure, capillary forces, and the specific geometry of PTFE fibers.

321　　**Insights from dimensionless number analysis**
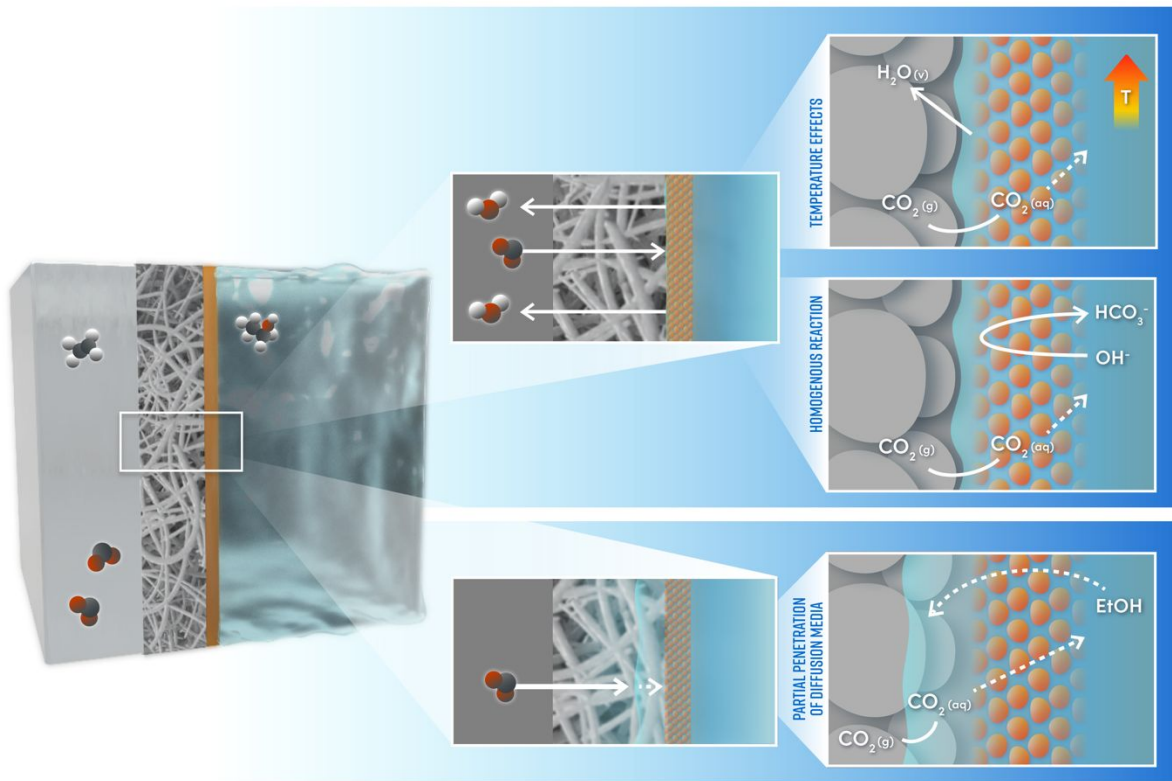
322

323　**Scheme 1.** Proposed phenomena that can impact CO_2 mass transport to the catalyst surface: temperature effects,
324　homogenous reaction, and partial penetration into diffusion media.
325

326　　　　We sought to use a single parameter that incorporates the aforementioned mass transport

327　mechanisms (Scheme 1) to better understand operating regimes. The Damköhler number, Da, is a

328　dimensionless quantity that represents the ratio between diffusion and reaction time scales. We

329　define Da to solicit a regime diagram for transport within the GDE (Eq. 1):

$$Da_{diff} = \frac{\tau_{DMl}}{[CO_{2,0}]P/m} = \frac{vP}{[CO_{2,0}]D_{CO_2}} \quad (1)$$

330

331　　　　Where *m* represents the molar consumption per unit area from reduction ($m = j/nF$, where

332　*j* is the current density), and *P* is the liquid penetration depth into the ePTFE. We performed a

333　timescale analysis representing diffusion of CO_2 to decouple activation- and mixed-controlled

334　regimes. When the timescale for CO_2 diffusion to the catalyst layer is greater than the timescale

335   for surface reactions, we define the system to be operating in a CO_2 mass transport limited regime

336   (Da > 1). As higher current densities are reached, the combination of mass transport limiting

337   mechanisms can push the system towards the Da > 1 regime.

338
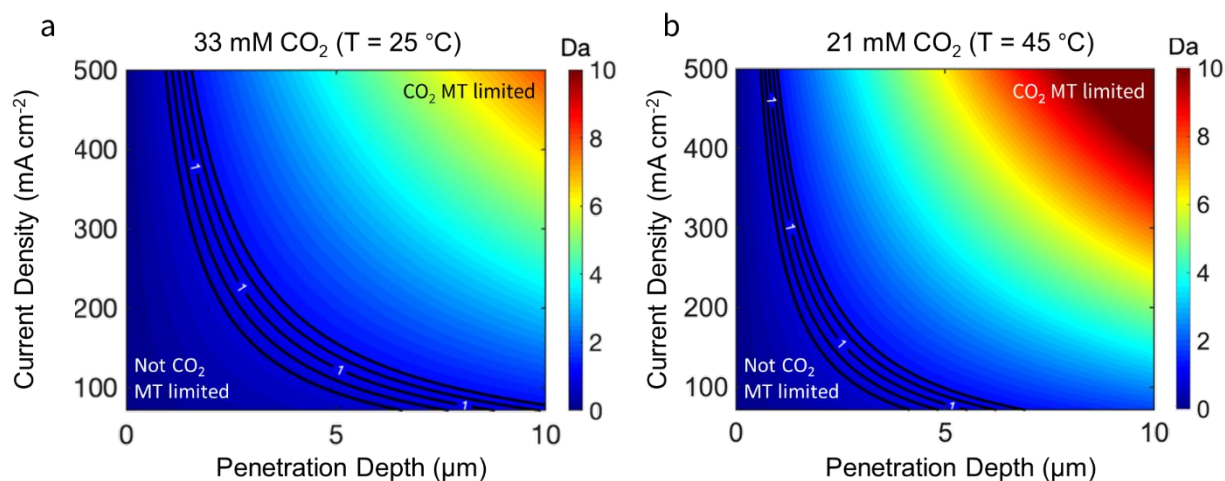
Fig. 6. Contour plots of Da, with contour lines at near the mass transport limitation boundary of Da~1 (Da=0.75-1.25),
representing two conditions for CO_2 concentration at the gas-liquid interface corresponding to (a) 33 mM (25°C) and
(b) 21 mM (45°C).

343   Contour plots (Fig. 6) elucidate different mass transport regimes based on CO_2 gas-liquid

344   interface concentrations of 33 (25°C) and 21 mM (45°C). For a system operating $\geq$ 100 mA cm^{-2}

345   with an interfacial CO_2 concentration of 33 mM (Fig. 6a), we predict that $\leq$ 5 μm of electrolyte

346   penetration will push the system towards a Da > 1 regime. As current density increases, this effect

347   is exacerbated due to increased OH^- generation. When extending this to lower interfacial CO_2

348   concentrations, we see the quantity of penetration to induce mass transport limitations is further

349   decreased. At 21 mM – a concentration corresponding to the temperature measurements during

350   electrolysis – the system enters the mass transport limited regime at $\leq$ 2 μm penetration at $\geq$ 100

351   mA cm^{-2} (Fig. 6b).

352   This model provides the framework for using Da as a relevant dimensionless number to

353   distinguish when a VFR is CO_2 mass transport limited for any reactor and system design. Other

354   additional variables, including the contributions from catalyst deformation, are not accounted in

355   this model; however, those effects are less likely to lead to our observations. Using Da to

356   understand the primary drivers and bottlenecks for species transport can lead to better design and

357   operation of reactors to overcome these limitations. Furthermore, AM presents a promising

358   platform for coupling with computational fluid dynamics for greater understanding of these

359   electrochemical systems.

360   **Achieving high yield of ethanol and ethylene in AMVFRs**
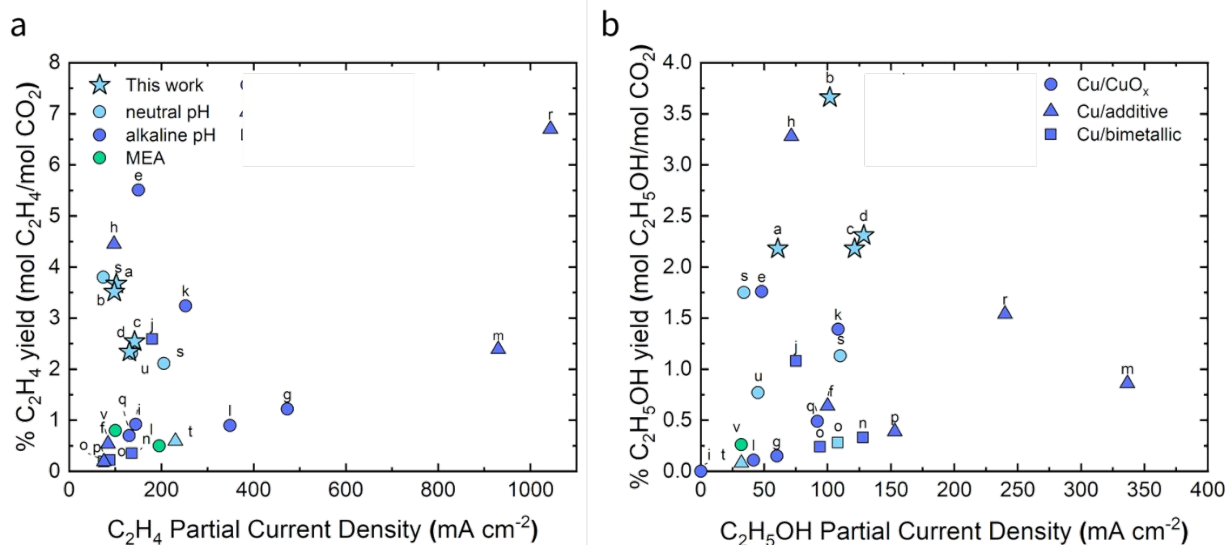
361
362   **Fig. 7.** Comparison of literature and this work for (a) % ethylene and (b) % ethanol yield as a function of partial
363   current density. Indigo colored data represents VFRs with bulk alkaline pH including [e] Ma et al.;[36] [f] Zhuang et
364   al.;[60] [g] Dinh et al.;[32] [h] Hoang et al.;[61] [i] Wang et al.;[37] [j] Hoang et al.;[38] [k] Lv et al.;[39] [l] Wang et al.;[62] [m]
365   Arquer et al.;[40] [n] Luo et al.;[35] [o] Li et al.;[63] [p] Wang et al.;[41] [q] Yang et al.;[64] [r] Ma et al..[42] Light blue colored
366   data represents VFRs with bulk neutral pH including [a-d] this work; [o] Li et al.;[63] [s] Tan et al.;[43] [t] Li et al.;[65] [u]
367   Ma et al..[33] Green colored data represents MEA VFRs including [l] Wang et al.;[62] [v] Garbardo et al..[66] Point shapes
368   represent catalyst layer composition class: Cu/Cu$_x$, Cu modified with a non-metal additive, and Cu-based bimetallics.
369
370   When assessing the feasibility of these systems, optimization of operating conditions and

371   system components toward specific products has seen significant advancements. However, this

372   does not account for the flowrate of CO_2 into the cathodic gas compartment; maximizing product

373   formation per molecule of CO_2 is imperative for improving the economic viability of CO_2

374   electrolysis. This ratio, known as yield, is defined for an CO_2R process below:

375
$$Yield = \frac{products\ out}{reactants\ in} = \frac{mol\ C_xH_yO_z\ produced}{mol\ CO_2\ in} \quad (2)$$

376   Product yield is critical as a primary metric to evaluate the reactor performance in many

377   industries. Considering the differences in catalyst composition and reaction area, local electrolyte

378   environment, and reactor and system design, we employ it here as a quantitative metric that can

379   be used to compare results from many reports across the field.

380   We compare the ethylene (Fig. 7a) and ethanol (Fig. 7b) yield for the highest performing

381   set of conditions from various reports. We classify the results from literature into three categories

382   for the electrolyte environment (neutral pH, alkaline pH, and membrane electrode assembly or

383   MEA) and three categories for the catalyst composition (Cu/CuO_x, Cu/additive, and bimetallics).

384   The AM VFRs in this work achieve high yield towards ethylene (3.67%), which is amongst the

385   highest performing systems for neutral electrolytes in literature (Fig. 7a). As expected, there is an

386   inverse relationship between product yield and CO_2 flow rate (Fig. S28).

387   On a partial current density basis, ethanol production is limited by challenging kinetics and

388   a focus on conditions that favor the competing ethylene pathway.[32,40,65] While various reports have

389   shown improved selectivity toward ethanol,[35,39,41] these findings are attributed to advanced catalyst

390   formulation and/or tuning of electrolyte and environment. With consistent production of ethanol

391   in AMVFRs across a range of CO_2 flow rates, we report the highest yield to date towards ethanol

392   (3.66%). This work affirms that high yield towards multi-carbon products from CO_2 can be

393   achieved with generic Cu catalysts in moderate electrolyte conditions.

Conclusions

394 In this work, we introduce a new paradigm for chemical production using advanced

396 manufacturing. We highlight prospects of AM for accelerated improvement and development of

397 CO_2 electrolyzers via reactor design; using 3D printing instead of conventional machining can lead

398 to significant improvements in activity, selectivity, yield, and energy efficiency through rapid

399 iteration. We realize reactor design, in addition to electrode and electrolyte engineering, as a key

400 variable for CO_2 reduction. Insights gained from this work can be employed for all vapor-fed

401 reactors to improve performance and build understanding.

402 The potential of this design strategy can lead to well-characterized and scalable systems,

403 especially when coupled with computational efforts and technoeconomic analyses. Furthermore,

404 we anticipate the implementation of AM for deterministic electrode, catalyst and membrane

405 development. This work demonstrates, for the first time, AM as a platform for creating robust

406 vapor-fed reactors and components for high-performance CO_2 reduction. We are optimistic that

407 AM will transform our approach towards designing systems for catalysis and propel the design of

408 novel reactors for the next generation of chemicals synthesis.

409

Author Contributions

D.C. and J.T.F. contributed significantly and equally to this work. *Writing – Original Draft:* D.C. and J.T.F; *Writing – Review & Editing:* D.C., J.T.F., S.S., J.D., D.L., A.A.W., A.S., C.H., T.F.J., S.B., and E.D.; *Conceptualization:* J.T.F., D.C., S.B., and E.D.; *Investigation:* D.C., J.T.F., J.D., D.L., and A.A.W.; *Methodology:* J.T.F., D.C., S.S., J.D., J.H. and V.A.B.; *Formal Analysis:* S.S., J.D., and V.A.B.; *Software:* V.A.B., S.S., J.D.; *Validation:* D.C., J.T.F., S.S., J.D., D.L., A.A.W., J.H., and V.A.B.; *Project Administration:* J.T.F., D.C., V.A.B., C.H., T.F.J., S.B., and E.D.; *Funding Acquisition:* A.S., C.H., T.F.J., S.B., and E.D.

Acknowledgements

Declaration of Interests

The authors declare no competing interests.

References

439   1. Obama, B. (2017). The irreversible momentum of clean energy. Science *355*, 126–129.

440   2. Intergovernmental Panel on Climate Change (2014). Clim. Change 2014 Synth. Rep.

441   3. Chu, S., Cui, Y., and Liu, N. (2017). The path towards sustainable energy. Nat. Mater. *16*, 16.

442   4. International Energy Outlook 2019 (2019).

443   5. De Luna, P., Hahn, C., Higgins, D., Jaffer, S.A., Jaramillo, T.F., and Sargent, E.H. (2019).
444   What would it take for renewably powered electrosynthesis to displace petrochemical
445   processes? Science *364*, eaav3506.

446   6. Hori, Y., Wakebe, H., Tsukamoto, T., and Koga, O. (1994). Electrocatalytic process of CO
447   selectivity in electrochemical reduction of CO2 at metal electrodes in aqueous media.
448   Electrochimica Acta *39*, 1833–1839.

449   7. Kuhl, K.P., Cave, E.R., Abram, D.N., and Jaramillo, T.F. (2012). New insights into the
450   electrochemical reduction of carbon dioxide on metallic copper surfaces. Energy Environ. Sci.
451   *5*, 7050.

452   8. Peterson, A.A., Abild-Pedersen, F., Studt, F., Rossmeisl, J., and Nørskov, J.K. (2010). How
453   copper catalyzes the electroreduction of carbon dioxide into hydrocarbon fuels. Energy
454   Environ. Sci. *3*, 1311–1315.

455   9. Zhang, M., Cheng, J., Xuan, X., Zhou, J., and Cen, K. (2017). Pt/graphene aerogel deposited
456   in Cu foam as a 3D binder-free cathode for CO2 reduction into liquid chemicals in a TiO2
457   photoanode-driven photoelectrochemical cell. Chem. Eng. J. *322*, 22–32.

458   10. Zhang, M., Xuan, X., Wang, W., Ma, C., and Lin, Z. (2020). Anode Photovoltage
459   Compensation-Enabled Synergistic CO2 Photoelectrocatalytic Reduction on a Flower-Like
460   Graphene-Decorated Cu Foam Cathode. Adv. Funct. Mater. *30*, 2005983.

461   11. Resasco, J., and Bell, A.T. (2020). Electrocatalytic CO2 Reduction to Fuels: Progress and
462   Opportunities. Trends Chem. *2*, 825–836.

463   12. Nitopi, S., Bertheussen, E., Scott, S.B., Liu, X., Engstfeld, A.K., Horch, S., Seger, B.,
464   Stephens, I.E.L., Chan, K., Hahn, C., et al. (2019). Progress and Perspectives of
465   Electrochemical CO $_2$ Reduction on Copper in Aqueous Electrolyte. Chem. Rev. *119*, 7610–
466   7672.

467   13. Mauri, R. (2015). Transport phenomena in multiphase flows (Springer).

468   14. Higgins, D., Hahn, C., Xiang, C., Jaramillo, T.F., and Weber, A.Z. (2019). Gas-Diffusion
469   Electrodes for Carbon Dioxide Reduction: A New Paradigm. ACS Energy Lett. *4*, 317–324.

470   15. Liang, S., Altaf, N., Huang, L., Gao, Y., and Wang, Q. (2020). Electrolytic cell design for
471   electrochemical CO2 reduction. J. CO2 Util. *35*, 90–105.

472   16. Vennekoetter, J.-B., Sengpiel, R., and Wessling, M. (2019). Beyond the catalyst: How
473   electrode and reactor design determine the product spectrum during electrochemical CO2
474   reduction. Chem. Eng. J. *364*, 89–101.

475   17. Gibson, I., Rosen, D., and Stucker, B. (2010). Additive Manufacturing Technologies. *238*.

476   18. Duoss, E.B., Weisgraber, T.H., Hearon, K., Zhu, C., Small IV, W., Metz, T.R., Vericella, J.J.,
477   Barth, H.D., Kuntz, J.D., Maxwell, R.S., et al. (2014). Three-dimensional printing of
478   elastomeric, cellular architectures with negative stiffness. Adv. Funct. Mater. *24*, 4905–4913.

479   19. Zhu, C., Liu, T., Qian, F., Chen, W., Chandrasekaran, S., Yao, B., Song, Y., Duoss, E.B.,
480   Kuntz, J.D., Spadaccini, C.M., et al. (2017). 3D printed functional nanomaterials for
481   electrochemical energy storage. Nano Today *15*, 107–120.

482   20. Nguyen, D.T., Meyers, C., Yee, T.D., Dudukovic, N.A., Destino, J.F., Zhu, C., Duoss, E.B.,
483   Baumann, T.F., Suratwala, T., Smay, J.E., et al. (2017). 3D-printed transparent glass. Adv.
484   Mater. *29*, 1701181.

485   21. Clark, E.A., Alexander, M.R., Irvine, D.J., Roberts, C.J., Wallace, M.J., Yoo, J., and Wildman,
486   R.D. (2020). Making tablets for delivery of poorly soluble drugs using photoinitiated 3D inkjet
487   printing. Int. J. Pharm. *578*, 118805.

488   22. Vericella, J.J., Baker, S.E., Stolaroff, J.K., Duoss, E.B., Hardin, J.O., Lewicki, J., Glogowski,
489   E., Floyd, W.C., Valdez, C.A., Smith, W.L., et al. (2015). Encapsulated liquid sorbents for
490   carbon dioxide capture. Nat. Commun. *6*, 1–7.

491   23. C. Bui, J., T. Davis, J., and V. Esposito, D. (2020). 3D-Printed electrodes for membraneless
492   water electrolysis. Sustain. Energy Fuels *4*, 213–225.

493   24. Yang, K., Kas, R., Smith, W.A., and Burdyny, T. (2021). Role of the Carbon-Based Gas
494   Diffusion Layer on Flooding in a Gas Diffusion Electrode Cell for Electrochemical CO2
495   Reduction. ACS Energy Lett. *6*, 33–40.

496   25. Zhang, J., Luo, W., and Züttel, A. (2019). Self-supported copper-based gas diffusion
497   electrodes for CO2 electrochemical reduction. J. Mater. Chem. A *7*, 26285–26292.

498   26. Ma, M., Clark, E.L., Therkildsen, K.T., Dalsgaard, S., Chorkendorff, I., and Seger, B. (2020).
499   Insights into the carbon balance for CO 2 electroreduction on Cu using gas diffusion electrode
500   reactor designs. Energy Environ. Sci. *13*, 977–985.

501   27. Hahn, C., Hatsukade, T., Kim, Y.-G., Vailionis, A., Baricuatro, J.H., Higgins, D.C., Nitopi,
502   S.A., Soriaga, M.P., and Jaramillo, T.F. (2017). Engineering Cu surfaces for the
503   electrocatalytic conversion of CO2: Controlling selectivity toward oxygenates and
504   hydrocarbons. Proc. Natl. Acad. Sci. *114*, 5918–5923.

505 28. Wang, L., Nitopi, S.A., Bertheussen, E., Orazov, M., Morales-Guio, C.G., Liu, X., Higgins,
506   D.C., Chan, K., Nørskov, J.K., Hahn, C., et al. (2018). Electrochemical Carbon Monoxide
507   Reduction on Polycrystalline Copper: Effects of Potential, Pressure, and pH on Selectivity
508   toward Multicarbon and Oxygenated Products. ACS Catal. *8*, 7445–7454.

509 29. Luo, M., Wang, Z., Li, Y.C., Li, J., Li, F., Lum, Y., Nam, D.-H., Chen, B., Wicks, J., Xu, A.,
510   et al. (2019). Hydroxide promotes carbon dioxide electroreduction to ethanol on copper via
511   tuning of adsorbed hydrogen. Nat. Commun. *10*, 1–7.

512 30. Liu, X., Schlexer, P., Xiao, J., Ji, Y., Wang, L., Sandberg, R.B., Tang, M., Brown, K.S., Peng,
513   H., Ringe, S., et al. (2019). pH effects on the electrochemical reduction of CO (2) towards C
514   2 products on stepped copper. Nat. Commun. *10*, 32.

515 31. Ma, S., Sadakiyo, M., Luo, R., Heima, M., Yamauchi, M., and Kenis, P.J. (2016). One-step
516   electrosynthesis of ethylene and ethanol from CO2 in an alkaline electrolyzer. J. Power
517   Sources *301*, 219–228.

518 32. Dinh, C.-T., Burdyny, T., Kibria, M.G., Seifitokaldani, A., Gabardo, C.M., de Arquer, F.P.G.,
519   Kiani, A., Edwards, J.P., De Luna, P., Bushuyev, O.S., et al. (2018). CO2 electroreduction to
520   ethylene via hydroxide-mediated copper catalysis at an abrupt interface. Science *360*, 783–
521   787.

522 33. Wang, Y., Shen, H., Livi, K.J., Raciti, D., Zong, H., Gregg, J., Onadeko, M., Wan, Y., Watson,
523   A., and Wang, C. (2019). Copper Nanocubes for CO2 Reduction in Gas Diffusion Electrodes.
524   Nano Lett. *19*, 8461–8468.

525 34. Hoang, T.T., Verma, S., Ma, S., Fister, T.T., Timoshenko, J., Frenkel, A.I., Kenis, P.J., and
526   Gewirth, A.A. (2018). Nanoporous Copper–Silver Alloys by Additive-Controlled
527   Electrodeposition for the Selective Electroreduction of CO2 to Ethylene and Ethanol. J. Am.
528   Chem. Soc. *140*, 5791–5797.

529 35. Lv, J.-J., Jouny, M., Luc, W., Zhu, W., Zhu, J.-J., and Jiao, F. (2018). A highly porous copper
530   electrocatalyst for carbon dioxide reduction. Adv. Mater. *30*, 1803111.

531 36. de Arquer, F.P.G., Dinh, C.-T., Ozden, A., Wicks, J., McCallum, C., Kirmani, A.R., Nam, D.-
532   H., Gabardo, C., Seifitokaldani, A., Wang, X., et al. (2020). CO2 electrolysis to multicarbon
533   products at activities greater than 1 A cm- 2. Science *367*, 661–666.

534 37. Wang, X., Wang, Z., García de Arquer, F.P., Dinh, C.-T., Ozden, A., Li, Y.C., Nam, D.-H.,
535   Li, J., Liu, Y.-S., Wicks, J., et al. (2020). Efficient electrically powered CO2-to-ethanol via
536   suppression of deoxygenation. Nat. Energy *5*, 478–486.

537 38. Ma, W., Xie, S., Liu, T., Fan, Q., Ye, J., Sun, F., Jiang, Z., Zhang, Q., Cheng, J., and Wang,
538   Y. (2020). Electrocatalytic reduction of CO2 to ethylene and ethanol through hydrogen-
539   assisted C–C coupling over fluorine-modified copper. Nat. Catal. *3*, 478–487.

540 39. Tan, Y.C., Lee, K.B., Song, H., and Oh, J. (2020). Modulating Local CO2 Concentration as a
541   General Strategy for Enhancing C- C Coupling in CO2 Electroreduction. Joule.

542   40. Yang, H., Hu, Y., Chen, J., Balogun, M.-S. (Jie T., Fang, P., Zhang, S., Chen, J., and Tong, Y.
543   (2019). Intermediates Adsorption Engineering of CO2 Electroreduction Reaction in Highly
544   Selective Heterostructure Cu-Based Electrocatalysts for CO Production. Adv. Energy Mater.
545   *9*, 1901396.

546   41. Feaster, J.T., Shi, C., Cave, E.R., Hatsukade, T., Abram, D.N., Kuhl, K.P., Hahn, C., Nørskov,
547   J.K., and Jaramillo, T.F. (2017). Understanding selectivity for the electrochemical reduction
548   of carbon dioxide to formic acid and carbon monoxide on metal electrodes. Acs Catal. *7*, 4822–
549   4827.

550   42. Luo, W., Nie, X., Janik, M.J., and Asthagiri, A. (2016). Facet Dependence of CO2 Reduction
551   Paths on Cu Electrodes. ACS Catal. *6*, 219–229.

552   43. Bagotsky, V.S. (2005). Fundamentals of Electrochemistry (John Wiley & Sons).

553   44. Lum, Y., Cheng, T., Goddard, W.A., and Ager, J.W. (2018). Electrochemical CO Reduction
554   Builds Solvent Water into Oxygenate Products. J. Am. Chem. Soc. *140*, 9337–9340.

555   45. Kuhl, K.P., Hatsukade, T., Cave, E.R., Abram, D.N., Kibsgaard, J., and Jaramillo, T.F. (2014).
556   Electrocatalytic Conversion of Carbon Dioxide to Methane and Methanol on Transition Metal
557   Surfaces. J. Am. Chem. Soc. *136*, 14107–14113.

558   46. Wang, X., Xu, A., Li, F., Hung, S.-F., Nam, D.-H., Gabardo, C.M., Wang, Z., Xu, Y., Ozden,
559   A., Rasouli, A.S., et al. (2020). Efficient methane electrosynthesis enabled by tuning local
560   CO2 availability. J. Am. Chem. Soc.

561   47. Luc, W., Fu, X., Shi, J., Lv, J.-J., Jouny, M., Ko, B.H., Xu, Y., Tu, Q., Hu, X., Wu, J., et al.
562   (2019). Two-dimensional copper nanosheets for electrochemical reduction of carbon
563   monoxide to acetate. Nat. Catal. *2*, 423–430.

564   48. Resasco, J., Lum, Y., Clark, E., Zeledon, J.Z., and Bell, A.T. (2018). Effects of anion identity
565   and concentration on electrochemical reduction of CO2. ChemElectroChem *5*, 1064–1072.

566   49. Weng, L.-C., Bell, A.T., and Weber, A.Z. (2018). Modeling gas-diffusion electrodes for CO$_2$
567   reduction. Phys. Chem. Chem. Phys. *20*, 16973–16984.

568   50. Wu, K., Birgersson, E., Kim, B., Kenis, P.J.A., and Karimi, I.A. (2014). Modeling and
569   Experimental Validation of Electrochemical Reduction of CO2 to CO in a Microfluidic Cell.
570   J. Electrochem. Soc. *162*, F23.

571   51. Delacourt, C., and Newman, J. (2010). Mathematical Modeling of CO2 Reduction to CO in
572   Aqueous Electrolytes: II. Study of an Electrolysis Cell Making Syngas from and Reduction at
573   Room Temperature. J. Electrochem. Soc. *157*, B1911.

574   52. Kas, R., Yang, K., Bohra, D., Kortlever, R., Burdyny, T., and Smith, W.A. (2020).
575   Electrochemical CO2 reduction on nanostructured metal electrodes: fact or defect? Chem. Sci.
576   *11*, 1738–1749.

577   53. Zong, Y., Chakthranont, P., and Suntivich, J. (2020). Temperature Effect of CO2 Reduction
578   Electrocatalysis on Copper: Potential Dependency of Activation Energy. J. Electrochem.
579   Energy Convers. Storage *17*.

580   54. Lobaccaro, P., Singh, M.R., Clark, E.L., Kwon, Y., Bell, A.T., and Ager, J.W. (2016). Effects
581   of temperature and gas–liquid mass transfer on the operation of small electrochemical cells for
582   the quantitative evaluation of CO 2 reduction electrocatalysts. Phys. Chem. Chem. Phys. *18*,
583   26777–26785.

584   55. Weng, L.-C., Bell, A.T., and Weber, A.Z. (2019). Towards membrane-electrode assembly
585   systems for CO 2 reduction: a modeling study. Energy Environ. Sci.

586   56. Leonard, M.E., Orella, M., Aiello, N., Roman-Leshkov, Y., Forner-Cuenca, A., and Brushett,
587   F. (2020). Editors' Choice—Flooded by Success: On the Role of Electrode Wettability in CO2
588   Electrolyzers that Generate Liquid Products. J. Electrochem. Soc.

589   57. Guancheng, J. (2018). Chapter 1 - Concept of Gas Wettability and Research Status. In Gas
590   Wettability of Reservoir Rock Surfaces with Porous Media, J. Guancheng, ed. (Gulf
591   Professional Publishing), pp. 1–27.

592   58. Zhuang, T.-T., Liang, Z.-Q., Seifitokaldani, A., Li, Y., De Luna, P., Burdyny, T., Che, F.,
593   Meng, F., Min, Y., Quintero-Bermudez, R., et al. (2018). Steering post-C–C coupling
594   selectivity enables high efficiency electroreduction of carbon dioxide to multi-carbon alcohols.
595   Nat. Catal. *1*, 421–428.

596   59. Hoang, T.T., Ma, S., Gold, J.I., Kenis, P.J., and Gewirth, A.A. (2017). Nanoporous copper
597   films by additive-controlled electrodeposition: CO2 reduction catalysis. ACS Catal. *7*, 3313–
598   3321.

599   60. Wang, Y., Wang, Z., Dinh, C.-T., Li, J., Ozden, A., Kibria, M.G., Seifitokaldani, A., Tan, C.-
600   S., Gabardo, C.M., Luo, M., et al. (2020). Catalyst synthesis under CO 2 electroreduction
601   favours faceting and promotes renewable fuels electrosynthesis. Nat. Catal. *3*, 98–106.

602   61. Li, Y.C., Wang, Z., Yuan, T., Nam, D.-H., Luo, M., Wicks, J., Chen, B., Li, J., Li, F., Garcia
603   de Arquer, F.P., et al. (2019). Binding site diversity promotes CO2 electroreduction to ethanol.
604   J. Am. Chem. Soc.

605   62. Yang, P.-P., Zhang, X.-L., Gao, F.-Y., Zheng, Y.-R., Niu, Z.-Z., Yu, X., Liu, R., Wu, Z.-Z.,
606   Qin, S., Chi, L.-P., et al. (2020). Protecting Copper Oxidation State via Intermediate
607   Confinement for Selective CO 2 Electroreduction to C 2+ Fuels. J. Am. Chem. Soc. *142*, 6400–
608   6408.

609   63. Li, F., Thevenon, A., Rosas-Hernández, A., Wang, Z., Li, Y., Gabardo, C.M., Ozden, A., Dinh,
610   C.T., Li, J., Wang, Y., et al. (2020). Molecular tuning of CO 2-to-ethylene conversion. Nature
611   *577*, 509–513.

612   64. Gabardo, C.M., O'Brien, C.P., Edwards, J.P., McCallum, C., Xu, Y., Dinh, C.-T., Li, J.,
613   Sargent, E.H., and Sinton, D. (2019). Continuous carbon dioxide electroreduction to

614   concentrated multi-carbon products using a membrane electrode assembly. Joule *3*, 2777–
615   2791.

616